Optics Letters

Chiral plasmonic metasurface absorbers in the mid-infrared wavelength range

MD. SHAMIM MAHMUD,[1] DANIEL ROSENMANN,[2] DAVID A. CZAPLEWSKI,[2] JIE GAO,[1,3] AND XIAODONG YANG[1,4]

[1]Department of Mechanical and Aerospace Engineering, Missouri University of Science and Technology, Rolla, Missouri 65409, USA
[2]Center for Nanoscale Materials, Argonne National Laboratory, Argonne, Illinois 60439, USA
[3]e-mail: gaojie@mst.edu
[4]e-mail: yangxia@mst.edu

Chiral metamaterials in the mid-infrared wavelength range have tremendous potential for studying thermal emission manipulation and molecular vibration sensing. Here, we present one type of chiral plasmonic metasurface absorber with high circular dichroism (CD) in absorption of more than 0.56 across the mid-infrared wavelength range of 5–5.5 μm. The demonstrated chiral metasurface absorbers exhibit a maximum chiral absorption of 0.87 and a maximum CD in absorption of around 0.60. By adjusting the geometric parameters of the unit cell structure of the metasurface, the chiral absorption peak can be shifted to different wavelengths. Due to the strong chiroptical response, the thermal analysis of the designed chiral metasurface absorber further shows the large temperature difference between the left-handed and right-handed circularly polarized light. The demonstrated results can be utilized in various applications such as molecular detection, mid-infrared filter, thermal emission, and chiral imaging. © 2020 Optical Society of America

https://doi.org/10.1364/OL.404192

Metamaterials exhibiting unique electromagnetic properties that are not available in natural materials can be tailored to develop functional devices for specific applications. One important application is that of metamaterial absorbers and thermal emitters working in the mid-infrared wavelength range [1–3]. Metamaterial absorbers in the mid-infrared range are suitable for applications including thermal imaging, low-cost molecular sensing, and thermophotovoltaics beyond the Shockley-Queisser limit [4–6]. However, most of the already-demonstrated mid-infrared metamaterial absorbers operate under linearly polarized light. Recently, metamaterial absorbers with chiroptical properties have drawn great attention because left-handed or right-handed circularly polarized (LCP or RCP) light can be selectively absorbed with high CD to exploit spin-dependent light-matter interactions. According to Kirchhoff's law, the emissivity of a material is equivalent to its absorptivity, so the thermal emissivity of a metamaterial can be predicted based on its light absorptivity. In a thermophotovoltaics system,

a wavelength-selective metamaterial thermal emitter with the resonance wavelength matching the semiconductor bandgap is required in order to obtain the optimal energy conversion efficiency [7]. Also, thermally stable metals and dielectrics like Au, Ti, W, and Al_2O_3 are usually used for building the metamaterial thermal emitters [8–10]. When considering circularly polarized thermal emission, the use of chiral metamaterial thermal emitters allows for further control of the response of a thermophotovoltaics system. In addition, mid-infrared metamaterial absorbers and thermal emitters can be used in low-cost gas or molecular sensing to detect CO_2 and PMMA molecules [11–13].

Depending on the choice of materials, three categories involving all-metallic, all-dielectric, and metal-dielectric metamaterial absorbers and thermal emitters can be designed [14,15]. Metal-dielectric metamaterial perfect absorbers or thermal emitters with the excitation of plasmonic magnetic resonances have been widely studied, where three-layer metal-insulator-metal structures are typically designed by integrating a top layer of metallic structures, a middle dielectric spacer, and a bottom metallic ground plane [1,16]. The plasmonic resonance wavelength of a metamaterial absorber or emitter can usually be tuned by varying the geometric parameters of the top metallic structure. Usually, the optical chirality of natural materials is weak. In order to resolve this issue, researchers have designed chiral metamaterials and metasurfaces with strong chiroptical responses. The recent progress of chiral metamaterial and metasurface design focuses on different types of asymmetric metallic structures such as spirals [17–19], Z-shaped slots [20], Z-shaped antennas [21], Gamma-shaped antennas [22], connected double bars [23,24], twisted elliptical holes [25], twisted semi-circles [26], gammadions [27], binary patterns [28], eye-shaped structures [29], and slanted apertures [30]. However, all of the above reported chiral metamaterials and metasurfaces operate at either visible or near-infrared frequencies. It will be important to design mid-infrared chiral metamaterial absorbers and thermal emitters for advancing the applications in thermophotovoltaics and molecular sensing. Recently, a planar-chiral plasmonic metasurface based on two coupled antennas was demonstrated

at mid-infrared frequencies due to the polarization-dependent Ohmic heat dissipation, but the obtained CD was low [31].

In this work, we present a new type of chiral plasmonic metasurface absorber based on the three-layer metal-insulator-metal structure operating in the mid-infrared wavelength range. The demonstrated chiral metasurface absorbers can selectively absorb the LCP or RCP incident light with a maximum chiral optical absorption of 0.87 and have the CD in absorption over 0.56 across the wavelength range of 5–5.5 µm, with the highest CD in absorption of 0.60. The observed high-efficiency chiral optical absorption and the large CD of the chiral metasurface absorbers are the result of the unique design of the top metallic structure. The chiral absorption resonant peak can be tuned to different wavelengths by simply changing the geometric parameters of the top metallic structure. In order to gather a better understanding of the mechanism involved in chiral optical absorption, electric field distributions are explained for both LCP and RCP incidence. Furthermore, the thermal analysis of the designed chiral metasurface absorber is conducted in order to predict the effect of the temperature difference between LCP and RCP illumination. These results provide new opportunities to develop chiral molecular sensing [32], polarization detection [21], chiral imaging [33,34], and thermal energy harvesting [7].

The unit cell of the designed plasmonic chiral metasurface absorbers is shown in Fig. 1(a), which represents the enantiomeric form with strong absorption of LCP light. The chiral metasurface absorber is designed with a three-layer gold-alumina-gold (Au-Al$_2$O$_3$-Au) structure, which includes the F-shaped structure resonators on the top 65 nm-thick Au layer, the middle 250 nm-thick Al$_2$O$_3$ dielectric spacer, and the bottom 200 nm-thick Au ground plane, which are deposited on a silicon substrate. The Au layers are deposited using a Lesker PVD 250 electron beam evaporator, while the Al$_2$O$_3$ layer is deposited by a Lesker CMS-18 reactive sputtering system. The F-shaped structures on the top Au layer are fabricated using a focused ion beam system (FIB, FEI Helios Nanolab 600, 30 kV, 28 pA). As shown in Fig. 1(b), the metasurface unit cell has the horizontal and vertical periods of $W = 2.08$ µm
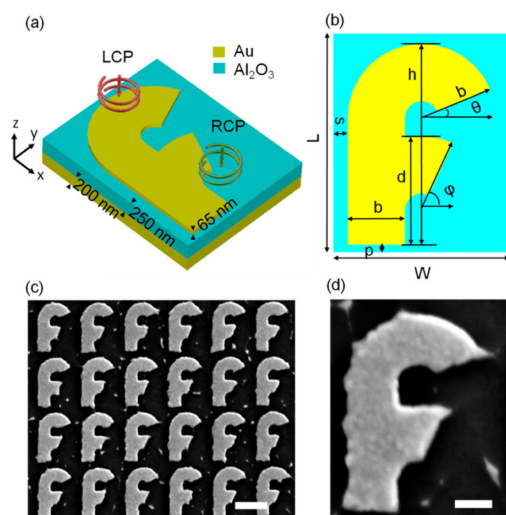
and $L = 2.57$ µm, respectively. The trust region framework algorithm is utilized for optimizing the geometric parameters of the asymmetric F-shaped structure in order to maximize the chiroptical response, which gives width $b = 675$ nm, upper arm height $h = 2.4$ µm, upper arm angle $\theta = 23°$, lower arm height $d = 1.28$ µm, lower arm angle $\varphi = 65°$, horizontal space $s = 165$ nm, and vertical space $p = 100$ nm. Figure 1(c) illustrates a scanning electron microscopic (SEM) top view image of the fabricated chiral metasurface absorber, and a zoomed-in SEM image of the unit cell is shown in Fig. 1(d).

In order to understand the mechanism of chiral optical absorption, electric field distributions are simulated for both LCP and RCP incidence using CST Studio Suite software, where periodic boundary conditions are applied around the unit cell in both x and y directions, while open boundary conditions are employed along z direction. A circularly polarized plane wave is vertically incident into the unit cell along z direction from the top. Only a 200 nm-thick silicon substrate is considered since the thick gold ground plane blocks almost all the transmitted light. The permittivity of alumina is obtained from the measured data [35] and the permittivity of gold is obtained from the Brendel-Bormann model [36]. Figure 2(a) displays the electric field $|E|$ distributions across the plane 30 nm above the lower surface of the top Au layer ($z = 480$ nm) and across the plane 200 nm above the lower surface of the Al$_2$O$_3$ layer ($z = 400$ nm) for both LCP and RCP light at the plasmonic resonance wavelength of 5.11 µm. It shows that for LCP incidence, the circularly polarized light is strongly coupled with the F-shaped resonator, and the electric field is concentrated around the metallic structure in the tip areas of both the upper and lower arms and also in the vertical space area, which results in low optical reflection and high absorption. However, for RCP incidence, the coupling between the incident circularly polarized light and the F-shaped resonator is weak and the majority of the incident light is reflected back, resulting in low absorption. Figure 2(b) further shows the electric field $|E|$ distributions across the plane at the tip of the upper arm ($x = 654$ nm) and across the plane right above the lower arm ($x = 1178$ nm) for both LCP and RCP light, where the locations of the two x planes are indicated by the white dashed lines marked in Fig. 2(a). It can be seen that the concentrated electric fields around the tip areas of both the upper and lower arms also greatly extend into the dielectric spacer for LCP incidence, proving strong optical absorption, but the optical mode in the spacer is much weaker for RCP incidence. The simulated CD in absorption defined as $CD = |A_{LCP} - A_{RCP}|$ for the optimized chiral metasurface absorber is 0.63, with the chiral optical absorption of 0.87 under LCP light at the resonance wavelength of 5.11 µm.

The resonance wavelength for chiral optical absorption can be easily tuned by varying the geometric parameters of the F-shaped structure. In order to cover the wavelength range from 5 to 5.5 µm, the geometric parameters marked in Fig. 1(b) for each metasurface absorber are scaled up by a factor of k^n, with the scaling constant $k = 1.027$ and the exponent $n = 0$, 1, 2, 3, while the upper arm angle $\theta = 23°$ and the lower arm angle $\varphi = 65°$ remain unchanged. A Fourier transform infrared spectrometer (FTIR, Nicolet 6700) connected to an infrared microscope is utilized to characterize the optical absorption spectra, with the circularly polarized light produced by a linear polarizer and a quarter-wave plate. Figure 3 plots the measured
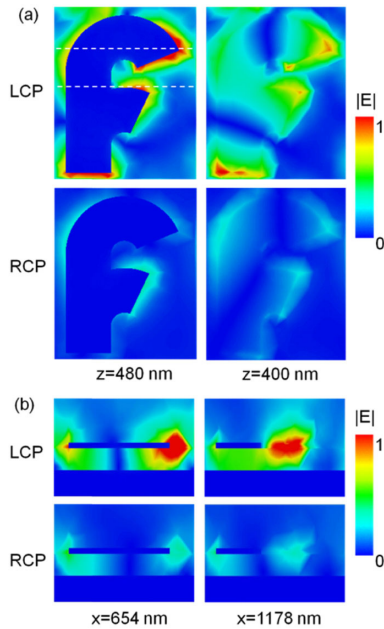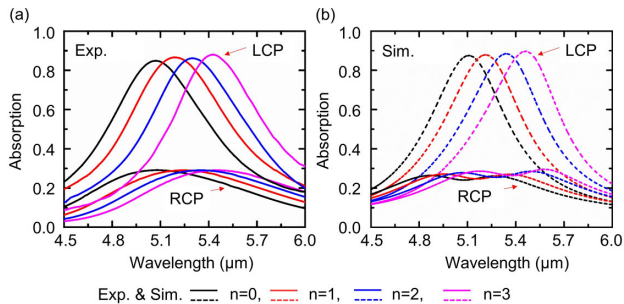

Fig. 1. (a) Schematic of the designed mid-infrared plasmonic chiral metasurface absorber. (b) Top-view schematic of the unit cell with the designed geometric parameters. (c) SEM image of the fabricated chiral metasurface absorber. Scale bar: 2 µm. (d) Zoomed-in SEM image of the unit cell. Scale bar: 500 nm.

Fig. 2. Simulated electric field distributions (a) in two z planes and (b) in two x planes under LCP and RCP incidence at the plasmonic resonance wavelength of 5.11 µm.

Table 1. Physical Properties of Materials Used for Thermal Analysis

	ρ (kg m^{-3})	C_p (J kg^{-1} K^{-1})	k (W m^{-1} K^{-1})
Gold	19320	129	315
Alumina	3970	765	1.6
Silicon	2330	712	148
Air	1	353[K]/T	0.03

Fig. 4. (a) Simulated temperature distributions in two z planes under LCP and RCP incidence at the resonance wavelength of 5.11 µm. (b) Temperature profiles along the black dashed line marked in (a) under LCP and RCP incidence.

and simulated optical absorption spectra from the chiral metasurface absorbers under both LCP and RCP incidence. It is clear that the resonance wavelength of chiral optical absorption continuously increases as n increases from 0 to 3. The absorption of LCP light is much stronger than that of RCP light, where the measured largest chiral optical absorption is 0.87 and the measured highest CD in absorption is 0.60 for the chiral metasurface absorber, with $n = 3$ at the resonance wavelength of 5.47 µm. The slight discrepancies between the measured and simulated absorption spectra in Fig. 3 are caused by the defects and sidewall roughness of the F-shaped structures introduced by the FIB milling process.
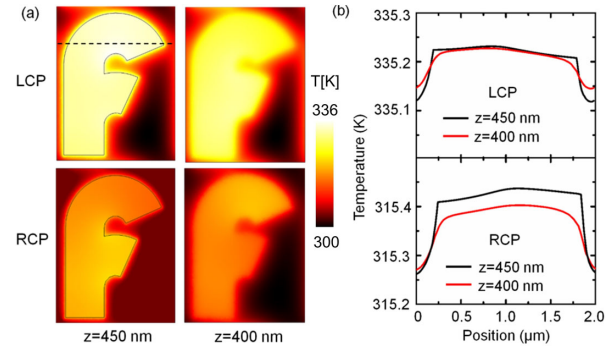
Furthermore, the temperature distribution in the chiral metasurface absorber is analyzed by solving the heat transfer equation $C_p \rho \, \partial T / \partial t + \nabla \cdot (-k\nabla T) = q$ using COMSOL Multiphysics software, where T is the temperature; C_p, ρ, and k are the specific heat capacity, density, and thermal conductivity of the material; and q is the heat generation density in metal with the expression of $q(r) = (\omega/2)\text{Im}[\varepsilon(\omega)]\varepsilon_0 |E(r)|^2$. In the thermal simulation, thermal insulation boundary conditions

Fig. 3. (a) Measured and (b) simulated optical absorption spectra of the chiral metasurface absorbers with the geometric scaled factor of k^n, where $k = 1.027$ and $n = 0, 1, 2, 3$ under LCP and RCP incidence.

are applied around the unit cell in both x and y directions. A 100 µm-thick silicon substrate is considered underneath the gold ground plane. The boundary conditions along z direction are set as a fixed temperature of 300 K at the top surface of air and the bottom surface of the silicon substrate. A circularly polarized plane wave is vertically incident into the unit cell along z direction from the top, where the incident optical power into one unit cell is 10 µW. The heat is mostly generated within the top F-shaped Au structure and then diffused to the surrounding materials at low temperature, until reaching thermal equilibrium. The thermal parameters used in this work are listed in Table 1 [23,37]. Figure 4(a) shows the simulated temperature distributions across the plane at the lower surface of the top Au layer ($z = 450$ nm) and across the plane 200 nm above the lower surface of the Al$_2$O$_3$ layer ($z = 400$ nm) for both LCP and RCP light at the resonance wavelength of 5.11 µm. It is shown that the temperature inside the F-shaped structure remains almost constant but higher than the surrounding materials due to the high thermal conductivity of gold. It can also be seen from Fig. 4(b) with the temperature profiles along the black dashed line marked in Fig. 4(a). The strong chiral optical absorption of the metasurface absorber causes the generation of more thermal energy and a significant local temperature increase inside the top-layer F-shaped metallic pattern for LCP incidence, with the highest temperature of 335.2 K. In comparison, the low optical absorption for RCP incidence results in the maximum local temperature of 315.4 K. The achieved large temperature difference of around 20 K between the LCP and RCP light is due to the strong CD in absorption in the designed chiral metasurface absorber.

In summary, chiral plasmonic metasurface absorbers have been designed and demonstrated to realize strong chiral optical absorption and high circular dichroism in absorption across

the mid-infrared wavelength range from 5 to 5.5 μm. The mechanism of strong chiroptical response of the designed chiral metasurface absorber is revealed by analyzing the electric field distributions under both LCP and RCP incidence. The resonance wavelength of chiral optical absorption is tuned by simply scaling up the geometric parameters of the unit cell structure. In addition, the thermal analysis is performed to predict the large temperature difference between the LCP and RCP light. These results are promising for future applications in chiral molecular sensing, polarization detection, chiral imaging, and thermal energy harvesting. Finally, it is worth noting that phase change materials such as germanium-antimony-tellurium alloy and vanadium dioxide can be introduced into the current chiral metasurface design to further actively tune and reconfigure the resonance wavelengths of mid-infrared chiral metasurface absorbers and thermal emitters [38].

Disclosures. The authors declare no conflicts of interest.

REFERENCES

1. N. I. Landy, S. Sajuyigbe, J. J. Mock, D. R. Smith, and W. J. Padilla, Phys. Rev. Lett. **100**, 207402 (2008).
2. Y. Cui, Y. He, Y. Jin, F. Ding, L. Yang, Y. Ye, S. Zhong, Y. Lin, and S. He, Laser Photon. Rev. **8**, 495 (2014).
3. H. Deng, Z. Li, L. Stan, D. Rosenmann, D. Czaplewski, J. Gao, and X. Yang, Opt. Lett. **40**, 2592 (2015).
4. E. Rephaeli and S. Fan, Opt. Express **17**, 15145 (2009).
5. H. A. Atwater and A. Polman, Nat. Mater. **9**, 205 (2010).
6. C. Wu, B. Neuner, III, J. John, A. Milder, B. Zollars, S. Savoy, and G. Shvets, J. Opt. **14**, 024005 (2012).
7. H. Deng, T. Wang, J. Gao, and X. Yang, J. Opt. **16**, 035102 (2014).
8. H. Wang, V. Prasad Sivan, A. Mitchell, G. Rosengarten, P. Phelan, and L. Wang, Sol. Energy Mater. Sol. Cells. **137**, 235 (2015).
9. D. Woolf, J. Hensley, J. G. Cederberg, D. T. Bethke, A. D. Grine, and E. A. Shaner, Appl. Phys. Lett. **105**, 081110 (2014).
10. D. Costantini, A. Lefebvre, A. L. Coutrot, I. Moldovan-Doyen, J. P. Hugonin, S. Boutami, F. Marquier, H. Benisty, and J. J. Greffet, Phys. Rev. Appl. **4**, 014023 (2015).
11. F. Cheng, X. Yang, and J. Gao, Sci. Rep. **5**, 14327 (2015).
12. A. Lochbaum, Y. Fedoryshyn, A. Dorodnyy, U. Koch, C. Hafner, and J. Leuthold, ACS Photon. **4**, 1371 (2017).
13. H. T. Miyazaki, T. Kasaya, M. Iwanaga, B. Choi, Y. Sugimoto, and K. Sakoda, Appl. Phys. Lett. **105**, 121107 (2014).
14. C. M. Watts, X. Liu, and W. J. Padilla, Adv. Mater. **24**, OP98 (2012).
15. T. Inoue, M. De Zoysa, T. Asano, and S. Noda, Optica **2**, 27 (2015).
16. X. Liu, T. Tyler, T. Starr, A. F. Starr, N. M. Jokerst, and W. J. Padilla, Phys. Rev. Lett. **107**, 045901 (2011).
17. M. Esposito, V. Tasco, M. Cuscunà, F. Todisco, A. Benedetti, I. Tarantini, M. D. Giorgi, D. Sanvitto, and A. Passaseo, ACS Photon. **2**, 105 (2015).
18. M. Esposito, V. Tasco, F. Todisco, A. Benedetti, D. Sanvitto, and A. Passaseo, Adv. Opt. Mater. **2**, 154 (2014).
19. J. K. Gansel, M. Thiel, M. S. Rill, M. Decker, K. Bade, V. Saile, G. von Freymann, S. Linden, and M. Wegener, Science **325**, 1513 (2009).
20. L. Kang, S. P. Rodrigues, M. Taghinejad, S. Lan, K.-T. Lee, Y. Liu, D. H. Werner, A. Urbas, and W. Cai, Nano Lett. **17**, 7102 (2017).
21. W. Li, Z. J. Coppens, L. V. Besteiro, W. Wang, A. O. Govorov, and J. Valentine, Nat. Commun. **6**, 8379 (2015).
22. B. Tang, Z. Li, E. Palacios, Z. Liu, S. Butun, and K. Aydin, IEEE Photon. Technol. Lett. **29**, 295 (2017).
23. L. Ouyang, W. Wang, D. Rosenmann, D. A. Czaplewski, J. Gao, and X. Yang, Opt. Express **26**, 31484 (2018).
24. L. Ouyang, D. Rosenmann, D. A. Czaplewski, J. Gao, and X. Yang, Nanotechnology **31**, 295203 (2020).
25. S. Wang, L. Kang, and D. H. Werner, Sci. Rep. **8**, 189 (2018).
26. Y. Cheng, F. Chen, and H. Luo, Phys. Lett. A **384**, 126398 (2020).
27. D.-H. Kwon, P. L. Werner, and D. H. Werner, Opt. Express **16**, 11802 (2008).
28. Z. Li, D. Rosenmann, D. A. Czaplewski, X. Yang, and J. Gao, Opt. Express **27**, 28313 (2019).
29. M. S. Mahmud, D. Rosenmann, D. A. Czaplewski, J. Gao, and X. Yang, Opt. Express **28**, 21192 (2020).
30. Y. Chen, J. Gao, and X. Yang, Nano Lett. **18**, 520 (2018).
31. A. B. Khanikaev, N. Arju, Z. Fan, D. Purtseladze, F. Lu, J. Lee, P. Sarriugarte, M. Schnell, R. Hillenbrand, M. A. Belkin, and G. Shvets, Nat. Commun. **7**, 12045 (2016).
32. E. Hendry, T. Carpy, J. Johnston, M. Popland, R. V. Mikhaylovskiy, A. J. Lapthorn, S. M. Kelly, L. D. Barron, N. Gadegaard, and M. Kadodwala, Nat. Nanotechnol. **5**, 783 (2010).
33. Q. Wang, E. Plum, Q. Yang, X. Zhang, Q. Xu, Y. Xu, J. Han, and W. Zhang, Light Sci. Appl. **7**, 25 (2018).
34. Y. Chen, X. Yang, and J. Gao, Light Sci. Appl. **7**, 84 (2018).
35. J. Kischkat, S. Peters, B. Gruska, M. Semtsiv, M. Chashnikova, M. Klinkmüller, O. Fedosenko, S. Machulik, A. Aleksandrova, G. Monastyrskyi, Y. Flores, and W. Ted Masselink, Appl. Opt. **51**, 6789 (2012).
36. A. D. Rakić, A. B. Djurišić, J. M. Elazar, and M. L. Majewski, Appl. Opt. **37**, 5271 (1998).
37. Z. Li, L. Stan, D. A. Czaplewski, X. Yang, and J. Gao, Opt. Express **26**, 5616 (2018).
38. N. Arash, W. Qian, H. Minghui, and T. Jinghua, Opto-Electron. Adv. **1**, 180009 (2018).